Flarescope Design Review

Ivey Davis

Abstract

Flarescope is a fully automated, 0.4 m telescope under development at Caltech and to be installed at Palomar Observatory. The major scientific goal for Flarescope is the monitoring of magnetically active dwarf stars of spectral type G and later with the intention of detecting continuum emission from highly energetic flares and the possible resultant coronal mass ejection (CME). This goal requires that Flarescope performs near continuous, sub-millimag ($\lesssim 500$ ppm), differential photometry. By looking at relatively red stars in comparatively blue bands (Sloan *u'* and *g'*) we expect to achieve high contrast detections (a ratio of flaring to quiet flux of ≥ 2) of flare events. On the Sun, such energetic flares also have associated metric radio emission in the form of Type II and III bursts, the former of which has origins intrinsic to CMEs and the latter of which is associated with solar energetic particle events, both of which have important consequences for the origins and development of life. This compels us to include low frequency ($\nu < 100$ MHz) observing as a part of our search for flare events through a coordinated observing system with the Long Wavelength Array. Here, we only focus on the design decisions and requirements of the optical component of the to-be coordinated system.

1 Introduction

Flarescope will be a fully autonomous instrument dedicated to sub-millimag (mmag), differential photometry of nearby, magnetically-active F, G, K, and M dwarfs. The goal is to produce high photometric precision light curves of target stars every night in order to detect low-contrast, non-periodic flares. Currently, it is planned to be a 0.4 m aperture telescope at the Palomar Observatory. In order for it to be fully autonomous, it will be able to identify that the weather is conducive for observing, control the dome, make an optimal observing schedule, choose the right filters, and perform the observations, data reduction, and photometry in real time without any manual input. Here, we describe the opto-mechanical and other decisions made in order to achieve mmag photometry and a fully automated system.

In Section 1.1 we review the science motivation for dedicated observations of magnetically active dwarfs and in 1.2 we review the decisions made regarding the optical train of the system to achieve high contrast, mmag differential photometry. In Sections 2, we review the hardware of the optical system (*e.g.* the telescope, mount, and CCD). Details for the dome, site and associated infrastructure, and observatory subsystems are provided in sections 3, 4, and 5 respectively.

1.1 Science Motivation

Many late type stars have been found to be incredibly magnetically active. A natural consequence of magnetic activity is large scale flares following magnetic reconnection events. For the Sun, if the energy released during such events is sufficient to overcome the containment of the surrounding plasma by the magnetic field, then we witness bulk plasma motion in the form of a coronal mass ejection (CME). For these sufficiently large flares, there are two major components of interest here– the consequential photospheric heating at the foot of the magnetic loops and the plasma emission associated with the CME. For the Sun, the latter component manifests in the form of Type II and complex Type III radio bursts. More specifically, these CMEs often drive shocks with frozen-in magnetic field lines. Should these shocks be super-Alfvénic ($v \approx 1000$ km/s), Type II bursts are produced. Complex Type III bursts originate from the electrons accelerated along the open field lines that drive the CME. The characteristics of Type II and III bursts are covered in detail by [3].

The strict origin of Type II bursts in CMEs make them an excellent tracer for CME events; a detection of a Type II burst is a detection of a CME. The coherent nature of the plasma emission mechanism also makes

these kinds of bursts incredibly bright at metric wavelengths (upwards of 10 GJy at $\sim$ 100 MHz). However, this corresponds to only $\sim$ 2.4 mJy at 10 pc. For a telescope like the Low Frequency Array (LOFAR), the Netherlands component of the array would only have a sensitivity of $\sim$ 13 mJy at 75 MHz assuming a bandwidth of 50 MHz and integration time of 10 minutes. Observing a CME would then require:

- Integrating over longer times and running the risk of averaging the burst flux out
- Integrating over longer bandwidths. However, 50 MHz is already at the upper end of bandwidth for low frequency observations and integrating over such large bandwidths also removes spectral information necessary for identifying the burst as Type II (namely, the frequency drift)
- Having a small volume sample of flare stars to observe
- Relying on extreme events
- Having a method other than Type II bursts to detect a CME

This final option motivates us to develop Flarescope for the sake of detecting the white light component of flares. This is the blackbody emission produced from photospheric back heating that produces hot spots with temperatures $\sim$ 9000 K [13], although much higher temperatures have also been reported for later spectral types [4]. The white light component of solar flares have been found to make up a significant fraction of the energy content of a flare [8], although the small contrast of the flare flux to the quiescent surface flux generally makes the white light component of a solar flare difficult to detect. This contrast is impacted by the relative temperature of the flare to the quiescent Sun – the smaller the temperature difference, the smaller the fractional flux increase– as well as the scale of the heated area– hot spots generally take up small areas and so can contribute significantly less to the total solar irradiance (TSI) than the quiescent surface. However, late type stars, particularly K and M dwarfs, can experience flares with temperatures comparable to or larger than solar flares. This factor, coupled with their lower surface temperature, would make the white light component of stellar flares from late type stars more obvious than for the Sun. This heightened contrast is further aided by the flares constituting a larger relative surface area on K and M dwarfs. By using relationships between the white light flare luminosity and kinetic energy of the flare, we hope to extrapolate estimates of the flare velocity – should it be super-Alfvénic (and by extension super-sonic since the fields of active regions responsible for producing flares can be 100s-1000s G), then the white light flare can be can be assumed to be associated with a CME.

Flarescope is being designed with the goal of detecting these white light flares in mind. Specifically, Flarescope is being designed to have mmag photometric precision on integration timescales of minutes in order to detect even low contrast flares from late type stars. Many of our restrictions are set by our main target of interest, ϵ Eridani (ϵ Eri), the closest sun-like star which also hosts an exoplanet[11]. ϵ Eri is a later type than our sun (K2) so that a flare from it will have a higher contrast than a flare of comparable energetics observed on the Sun. ϵ Eri is also much younger than the Sun (only a few hundred million years[11]), has a stronger magnetic field (surface strength of $\sim$ 160 G[14]), and has a rotation period of 11 days [5]. The combination of these features makes ϵ Eri an especially magnetically-active star. The plasma environment of ϵ Eri and the space weather that ensues from frequent, large flares is of interest especially in the context of the habitability of ϵ Eri's exoplanet. The goal of Flarescope is then to detect flares from ϵ Eri, as well as other magnetically active stars (see Section 1.1.1), in order to identify CMEs, characterize the plasma environment of the stars, and evaluate the impact that stellar activity of sun-like and later-type stars has on habitability.

While the design of Flarescope is motivated by the white light component of flares, it will also work in a coordinated fashion with the Long Wavelength Array (LWA) at the Owens Valley Radio Observatory (OVRO) in hopes of also detecting for the first time a stellar analog of the Type II and III bursts. This will help with characterizing the timeline of emission processes of stellar flares in order to better understand how stellar flare dynamics may differ from solar flares as well as aid in identifying whether or not the flare is associated with a CME. Further, because stellar flares are not known to experience periodicity, observing as frequently and continuously as possible is key for flare detection. With these requirements in mind, the technical goal of Flarescope is then for all observing tasks (weather assessment, dome and telescope control and telemetry, scheduling, imaging, data reduction, and flare identification) to be fully automated.

Star	Sp. Type	d [pc]	$m_{g'}$	Field Reference	$m_{g'}$	Separation [amin]	Transit χ	Notes
ϵ Eri	K2	3.2	4.1	HD 22130	9.65	11.94	1.36	Nearby, active, planet host
GX And	M2	3.6	9.1	BD+43 48	9.73	1.18	1.02	Eruptive variable, planet host
κ^1 Ceti	G5	9.2	5.11	BD+02 521	8.97	4.45	1.15	BY Dra, 9 day rotation period, superflare candidate
12 Oph	K1	9.9	6.09	HD 149476	9.65	18.09	1.22	By Dra
EQ Peg	M4+M5	6.2	10.93	CCDM J23322+1942AB	9.76	14.74	1.03	UV Ceti type
AD Leo	M3	4.9	10.13	BD+20 2464	11.03	1.50	1.03	UV Ceti type, planet host candidate
UV Ceti	M6	2.7	13.75	TYC 5855-1883-1	12.25	13.1	1.59	UV Ceti type
WX UMa	M6	4.9	15.45	TYC 3012-425-1	12.04	8.70	1.02	UV Ceti type
Gl 380	K6	4.9	7.23	HD 233714	9.52	2.54	1.04	Eruptive variable, 1.7 day rotation period, possible planet host
Gl 892	K3	6.5	6.00	HD 240224	9.34	9.00	1.09	Eruptive variable, hosts 6 planets
CF UMa	K1	9.2	6.75	BD+38 2286	10.24	8.78	1.00	Superflare candidate

Table 1: List and details of the initial target stars for Flarescope.

1.1.1 Target Objects

The initial list of objects of interest is given in Table 1. The two main restrictions we set for our targets is that they be magnetically active dwarfs and that they be nearby ($d \lesssim 10\,\mathrm{pc}$). There are two main groups of stars satisfying these requirements: 1.) active G, K, and early M type stars and 2.) mid and late type, fully-convective M dwarfs. The distinction is important; UV Ceti type variables have incredibly strong fields, upwards of several kG, making the Alfvén speed highly relativistic and the energies required to escape magnetic confinement enormous. Because of this, it is unclear that these stars would be capable of producing a CME, despite producing some of the most powerful stellar flares. However, as such late spectral types with such powerful flares, these targets offer the best possible white light contrasts and possibility of observing non-CME-associated radio emission (*e.g.* other Type III burst emission and other plasma emission at many stellar radii). For such cool stars, the habitable zone is also much closer to the star, making any planets within the habitable zone more susceptible to the impact of the flare (be that organic compound genesis or sterilization of the surface). Because of the considerable impact that these stars have on their environment irrespective of producing CMEs, we include them as targets of interest for Flarescope.

The first group of targets of interest pose an observational challenge and drive many of the restrictions for Flarescope's design. As hotter stars (at least relative to the late M dwarfs), the white light components of observed flares will have a comparably smaller contrast (see Section 2.4 and Figure 4). This sets the requirement of being capable of mmag photometry and, as discussed in Section 1.2, sets filter, field of view (FOV), and additional optics restrictions. However, observing magnetically active, solar-like stars–especially those with planets– is of particular interest. These stars have fields much stronger than the Sun's while also weaker than the UV Ceti variables (*i.e.* between a few 10s to few 100s G) that should produce strong flares by solar standards that are also capable of reaching super-Alfvénic speeds and therefore capable of producing CMEs and associated shocks. For this reason, ϵ Eri, which is the nearest sun-like star with an exoplanet, is the main target of interest for Flarescope.

1.2 Technical Requirements

In order to be sensitive to as low contrast flares as possible, Flarescope has been designed with the goal of performing sub-millimag ($\sigma_{\mathrm{phot}} \lesssim 1000\,\mathrm{ppm}$), differential photometry. This limit for Flarescope is driven by the 2003 Halloween solar storm, where the TSI increased by 270 ppm during an X 17 class flare [18], which would suggest a 440 ppm increase for the X 28 flare that happened during that same period. We would then expect for a star like ϵ Eri which has a bolometric flux $\sim 1/3$ that of the Sun to increase in bolometric brightness by $\sim 1\,\mathrm{mmag}$ for a comparably energetic flare. For a flare bolometric luminosity comparable to the quiescent luminosity of ϵ Eri, this value is enhanced by a factor of 2 by observing in the g' band so that 500 ppm precision is nearly a 5σ detection.

The endeavor of affordable, ground-based mmag precision is not new ([15, 16, 17, 10, 9]). The limiting factor of any ground-based telescope with such a goal will be scintillation, the phenomenon of which is covered in detail in [12]. The expression for scintillation noise σ_S is given in equation 1 [12], where the factor of 1.5 follows from the original expression for σ_S being underestimated by about a factor of 1.5 [7]. In this equation, D is the diameter of the telescope in cm, χ is the airmass, t_{int} is the integration time, h is the elevation of the telescope in m, and h_0 is taken to be 8000 m. Flarescope will be located at the Palomar observatory and so h is taken to be 1712 m. This expression is plotted as a function of airmass and exposure

	CDK 17	**CDK** 20
Pixel Scale/FOV	0.91"/15.58'	0.78"/13.25'
Time required (s)	381	315
Required pixel diffusion	1167	1572
Dimmest Object ($m_{g'}$)	11.72	12.03
Cost	\$19,500	\$29,500

Table 2: Comparison of the 17" and 20" CDK telescopes being considered. The time required is the integration time required to reach ppm precision given the required diffusion and for sources with mag $\lesssim 10.5$ (*i.e.* in the scintillation dominated regime) and the required pixel diffusion is the number of pixels we would have to diffuse over for ϵ Eri to not saturate the detector in the time it takes to read out an image (we define saturation as 1/2 the well depth of the detector, *i.e.* 45,000 e^-). The dimmest object is the g' magnitude of the dimmest object that will saturate the detector in 1 s

time in Figure 1.

$$\sigma_S = 1.5 \times 0.09\, D^{-2/3} \chi^{1.75} \left(2\, t_{\rm int}\right)^{-1/2} \exp(-h/h_0) \tag{1}$$

Scintillation dominates total noise for bright sources and so, along with the targets and physical limitations of the CCD, guides many of our optics decisions. Additionally, being able to do differential photometry requires that there be an adequate photometric companion within the same field and thus favors a large FOV. This restriction further impacts our decisions for Flarescope hardware. In this section, we will discuss our justification for the telescope hardware for Flarescope while in Section 2 we will give more details on each component in addition to computation details.

1.2.1 Photometric Precision

Our photometric precision (as well as FOV) considerations start with our decision to get a corrected Dall Kirkham (CDK) telescope. Compared to a Ritchey–Chrétien, the optical train of a CDK allows for a larger FOV free of optical errors. The two main telescopes of consideration were the PlaneWave CDK 17 (0.43 m aperture) and PlaneWave CDK 20 (0.50 m aperture), the major differences of which are summarized in Table 2. Although the CDK 20 would have lower overall noise and hence would achieve mmag photometry on shorter timescales than the CDK 17, its two downfalls relative to the CDK 17 are its smaller FOV and the number of pixels that would have to be diffused across to avoid saturating the detector for our brightest targets. Considering that flares can last 10s of minutes, the extra $\sim$ 1 minute needed to reach mmag precision with the CDK 17 is not much of a sacrifice compared to what would be lost (both photometrically and monetarily) with the CDK 20.

Another important source of noise that we included in our decisions was that introduced by the electronics. In particular, in order to mitigate confusion due to pixel-specific response of the EMCCD, we will use an equatorial mount (Section 2.2) and an autoguiding system (Section 2.6). The use of an equatorial mount rather than an Alt-Az mount ensures that the target star and its photometric companion don't rotate across the EMCCD throughout the observation. The use of an autoguiding system allows for sub-arcsecond tracking so that the objects stay on the same pixels for the entire night. In addition to mitigating confusion due to pixel-specific responses, this also makes the data reduction process much easier as the psf will be in the same location for each frame; the pixel position of the relevant objects do not need to be located for each frame.

Finally, for our brightest stars like ϵ Eri, we run the risk of saturating the detector faster than it can be read out. Others have gotten around this issue by defocusing the telescope to diffuse the light [17, 16]. However, the psf of the defocused light is complex and makes aperture photometry difficult. In order to exercise more control over the psf while also diffusing light, we will use engineered diffusers. When placed appropriately in the optical train, this piece can produce a top-hat psf in principle as large as needed, allowing for sufficiently long exposures with a simple psf. Using the diffuser in tandem with a filter requires a dual filter wheel. The filter wheel we will use for Flarescope is the FLI-CL1-10. Because we do not want to use the diffuser for especially dim objects, the FLI-CL1-10 being mechanical rather than manual so we can decide which objects we want to use the diffuser on– in addition to being able to accommodate the 50 mm square diffuser– was a key factor in our decision for the wheel.

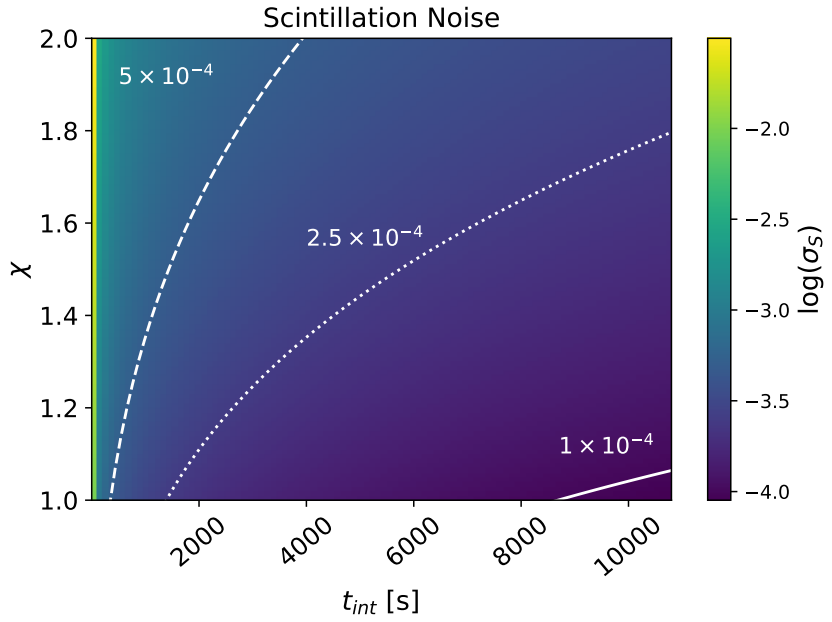

Figure 1: Equation 1 as a function of air mass and magnitude. The dashed, dotted, and filled line represent the parameter space that support σ_S of 5×10^{-4}, 2.5×10^{-4}, and 10^{-4} (~ 0.5, 0.3, 0.1 mmag) respectively.

Finally, it is important to note that there is a tradeoff between high contrast imaging and good photometry that manifests in our filter selection. For a ~ 9000 K flare, we would get the highest contrast in the u' band (center wavelength ~ 350 nm). However, the efficiency of the lenses and CCD as well as the atmospheric transmissivity is severely diminished in this band when compared to the g' band (center wavelength ~ 475 nm). Due to the throughput of the optical system in the g' band ($\gtrsim 2\times$ that of the u' band), the g' band will be our primary science band, although we will also have the u', r', and i' filters for additional science purposes. More discussion of the filters is provided in Section 2.4.

1.2.2 Field of View

The three major contributors to the FOV are the diameter of the aperture, the focal length, and detector size. Since we are using a contributed EMCCD, our ability to increase the FOV is limited to the diameter and the focal length. Both the CDK 17 and CDK 20 PlaneWave telescopes have an $F\# = 6.8$, leading us to again favor the CDK 17, which has an FOV $\sim 1.2\times$ that of the CDK 20.

PlaneWave has a $0.66\times$ focal reducer designed specifically for their CDK telescopes that would increase the FOV of the CDK 17 to $23.8' \times 23.8'$ (assuming our 1024×1024 pixel EMCCD; see Section 2.5). However, we can instead expand the allowable distance between target and companion by using the PlaneWave integrated rotational focuser (IRF90) in place of the Hedrick focuser. Using the IRF90 allows us to use the diagonal of the detector, expanding the allowed separation between the target and companion from $15.7'$ to $22.2'$. This is only $\sim 1.6'$ less than that offered by the focal reducer alone, and does not suffer from additional throughput loss and degraded psf as the focal reducer would.

Component	Cost	Notes
Site Clearing and Pad	$15,000?	
Palomar Staff		
Telescope[1] + Wedge[2]	$47,586	120 V
IRF90[3]	$4,500	90 mm aperture and 40 lb (18 kg) payload
Dome[4]	$48,500	230 V, single phase
Flat Concrete Adapter Plate	$800	
Dual filter wheel[5,6]	$2,595	FLI 10 position dual filter wheel. 5.3 lb, 12 V
Sloan filter set[7]	$550/filter, $2,200 total	u', g', r', and i' filters
Diffuser (2" sq)[8]	$500/diffuser, $1,500 total	0.25°, 1°, and 2° diffusion angles
CCD (Andor iXon3 888[9])	(Contributed)	Operating power: < 95 W, 100-240 VAC
Guidescope[10]	$823	51 mm RedCat telescope
Guide camera[11]	$149	ASI 120 mm CMOS camera
Autoguiding system[12]	$279	ZWO ASIAir Pro
Autoguider Auto Focuser[13]	$248	ZWO ASIAir Pro Electronic Auto Focuser (EAF). 5V. 0.5 lbs
Operational CPU	$2,034	See Table 6
Analysis CPU	$6,671	See Table 6
HVAC	$4,000	4X NEMA rated enclosure, 800 BTU/hr heat capacity support
Weather Station[14]	$635	Wireless Vantage Vue Weather Station + Console and mounting pole kit
Total	$137,520	

Table 3: A summary of the hardware and other expenses associated with Flarescope.

2 Hardware

2.1 Telescope

Flarescope will be a 0.43 m PlaneWave observatory system (CDK 400; see Figure 3) which includes the CDK 17 optical tube and L 500 direct drive mount. This particular telescope is nominally an Alt-Az mount,

[1] CDK 400 observatory
[2] L500 wedge
[3] Integrated rotating focuser
[4] Astrohaven dome
[5] FLI Cl1-10 position dual filter wheel
[6] Additional information for FLI CL1-10 FW
[7] Sloan filters
[8] Engineered Diffuser
[9] Andor iXon3 888
[10] 51 mm RedCat guidescope
[11] ASI 120 mm CMOS camera
[12] ZWO ASIAir Pro
[13] ZWO ASIAir EAF
[14] Wireless Vantage Vue bundle

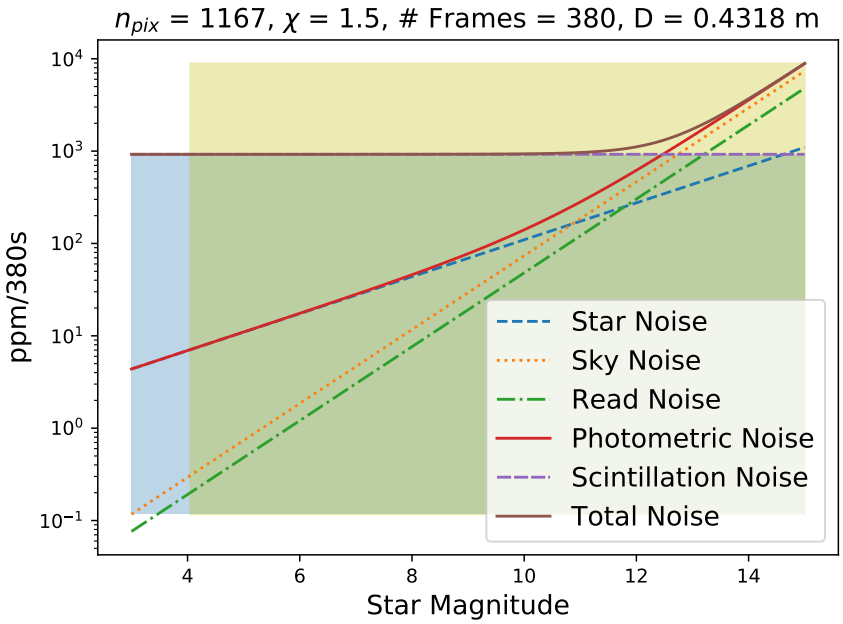

Figure 2: Different noise values in ppm as a function of the companion star's magnitude. The blue region represents noise $\leq$ 1mmag and the yellow region is the star magnitudes which won't saturate the detector in a 1 s integration. The $n_{\rm pix} = 1167$ is found from assuming a psf size so that ϵ Eri won't saturate the detector in the time it takes to readout a frame at 1 MHz. 500 precision would then require $\sim$ 25 mintes.

but we will use the L 500 equatorial wedge to make it equatorial. The lenses will be quartz with anti-reflection (AR) coatings to optimize throughput in the 300-400 nm range (transmission nearly 100% in the u' and g' bands). The CDK design removes effects such as coma, off-axis astigmatism, and field curvature for fields $\lesssim 1°$.

2.2 Mount

We will be using the L 500 direct drive mount which has a payload capacity of $\sim$ 200 lbs (about 2$\times$ the CDK 17 optical tube weight of 106 lbs). The slew speed can be as high as 50°/s; although it is unlikely we will use such a high slew speed, the fact that the instrument can move so fast necessitates an alert system for when the telescope slews to new targets. The sidereal tracking accuracy is $<$ 0.3" rms over 5 minutes (this will be supplemented with an autoguiding system; see Section 2.6). This mount is controlled via the PlaneWave Interface (PWI4) software which, given that it is ASCOM compliant, will be compatible with the autoguiding system we will be using.

2.3 Focuser

We will be using the IRF90 integrated rotating focuser in order to maximize the available FOV as described in 1.2.2. In addition to this benefit, it is also capable of supporting a larger payload than the Hedrick focuser (40 lbs capacity versus 20 lbs). It has a 365 degree range with hardstops to avoid the possibility of cord wrap. This focuser requires an electronic focus accessory (EFA) which operates through PWI3. The EFA not only automatically controls the focusing, but also monitors the temperature of the observatory system and controls the fan of the telescope.

Figure 3: The PlaneWave CDK 400 observatory (left) and AstroHaven dome (right)

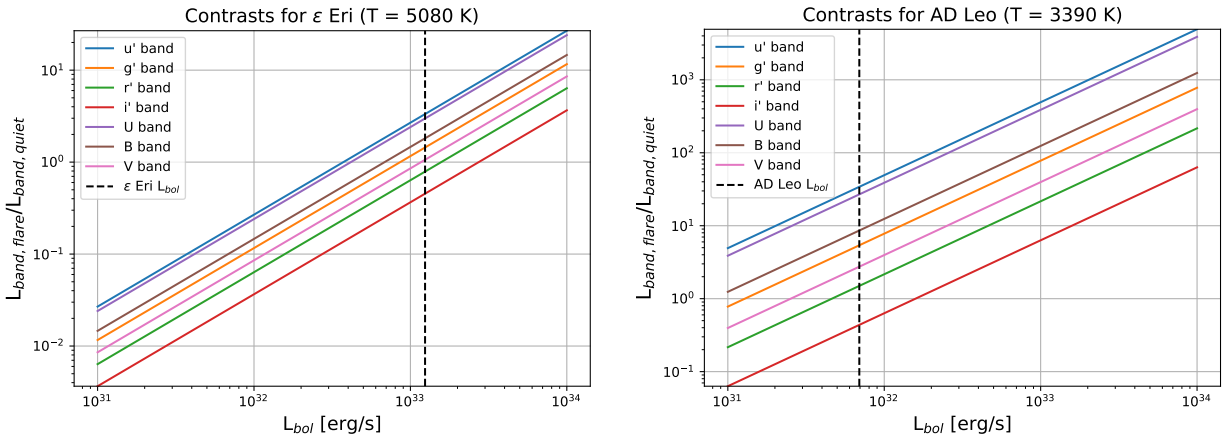

Figure 4: The ratio of the flaring luminosity to the quiescent luminosity of ϵ Eri (left) and AD Leo (right) in a band as a function of the flare's bolometric luminosity assuming a flaring temperature of 9000 K.

2.4 Filters and Filterwheel

The blackbody nature of the white-light flare component means that achieving the highest contrast requires observing in the bluest bands; although our target stars have temperatures between about $2700 - 5000\,\mathrm{K}$, a flaring temperature of $9000\,\mathrm{K}$ puts the peak emission at $\sim 330\,\mathrm{nm}$ which lies in the Sloan u' band. While the u' filter would provide the highest flaring contrasts (see Figure 4), the low atmospheric transmission in the band due to absorption from ozone [6] as well as the diminished quantum efficiency of the CCD at these wavelengths leads us to favor the g' band. For a flaring luminosity comparable to the quiescent luminosity of ϵ Eri, the brightness of the flare is only slightly greater than the quiet photosphere in the g' band as shown in Figure 4. However, it is possible for there to be flares with bolometric luminosities greater than the quiescent luminosity of the host and ϵ Eri itself is one of the earliest spectral types we intend to look at; although ϵ Eri is our main target of interest and is setting important restrictions on the telescope design, it is certainly not the star from which we expect the highest contrast. Additionally, for mmag sensitivity, we should be able to detect a flare $\sim 10^{30}\,\mathrm{erg/s}$, which again is well within the realm of possibility for an active star with high magnetic filling factors like ϵ Eri[2].

While Flarescope will focus largely on the u' and g' bands, it will also have r' and i' filters available for observations unrelated to its main science goal. Additionally, we intend to eventually utilize a dichroic and H α filter in order to measure the radial velocity of ejected plasma. Such measurements would put better restrictions on whether the observed flare is associated with a CME, but since this particular instrumentation won't be apart of the initial phase of Flarescope, we will exclude further discussion on the subject here.

The FLI-CL1-10 filter wheel (see footnote 5) has 8+2 positions between the two carousels, allowing for simultaneous use of a diffuser and filter if observing bright objects. This filter wheel operates through the Finger Lakes Instruments software development toolkit.

2.4.1 Diffusers

We will be getting three diffusers with 0.25°, 1°, and 2° diffusion angles. The 1° diffuser will set the placement of the filterwheel in the optical train relative to the CCD; its goal is to diffuse ϵ Eri across the 1167 pixels necessary so that ϵ Eri does not saturate the detector in the time it takes to read it out at the 1 MHz readout rate. At the distance set by this requirement, the 0.25° then provides diffusion across 74 pixels (corresponding to a limiting magnitude of 7.0) and the 2° provides diffusion across 4681 pixels (limiting magnitude of 2.5). The use of a 0.25° diffuser is helpful for sources that would still saturate the detector without a diffuser, but for which a 1° diffusion angle would introduce unnecessarily high read noise. The 2° diffuser is being purchased in anticipation of there being sources brighter than ϵ Eri that we may want to observe in the future.

2.5 CCD

We will be using the Andor iXon3 888 EMCCD; its operating information is provided in Table 4. In addition to these details, this EMCCD is backlit– giving it a higher quantum efficiency than a front-illuminated CCD (see Figure 5)– and is a frame transfer CCD, allowing for simultaneous imaging and read out. This EMCCD is also thermoelectrically cooled (TEC), making our HVAC requirements much more manageable since we will not rely on glycol to keep the detector cool enough that dark current is essentially negligible.

2.6 Guiding

Due to the restrictions set by scintillation, Flarescope requires integration times on the order of several minutes to reach mmag sensitivity. Then, in order to keep the psf of the target and companion star on the same pixels throughout this duration, we will be using a closed loop guiding system. Specifically, we will be using the ZWO ASIAir, which is capable of independent autoguiding and imaging. This will be mounted on the RedCat 51 mm telescope (F# = 4.9, PS = 0.825"/micron) along with the ASI 120 mm CMOS camera ($1280 \times 960\,\mathrm{px}$, 3.75 micron/px, see Table 5 for more information) giving a FOV of $66.0' \times 49.5'$. A FOV of this scale should be sufficiently large to find a bright star to guide with for any field. Given that the ZWO ASIAir is an autoguider, at each new field that the PlaneWave (and consequently the mounted RedCat) telescope points to the ASIAir will automatically select the best guide star in the field.

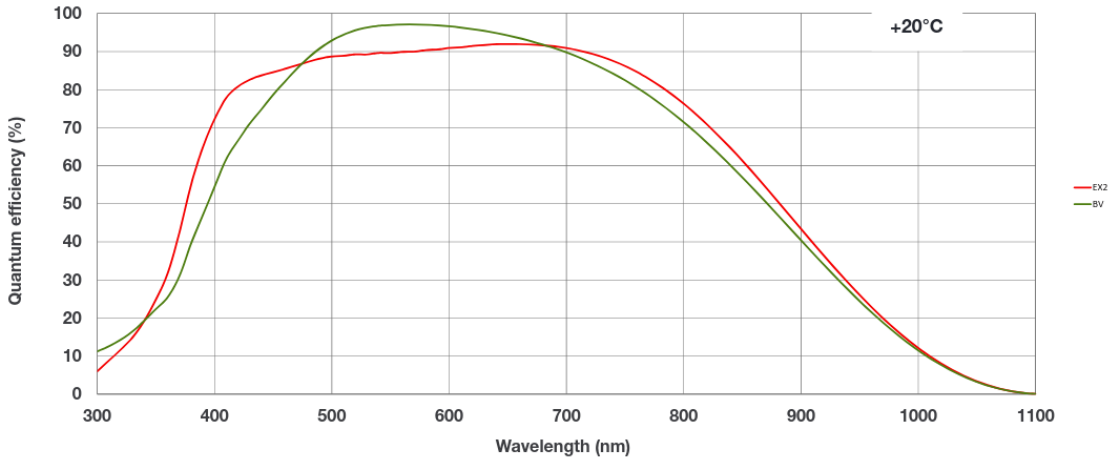

Figure 5: Quantum efficiency of the Andor iXon EMCCD (see footnote 9). BV refers to the standard AR, mid-band coating and EX2 refers to a dual coating. The EX2 is only available for the iXon Ultra and so is not relevant for our CCD. There's a strong drop in efficiency below 500 nm and an even steeper drop off below about 400 nm. Given that the u' band is between about 320 and 380 nm, we are compelled to use the g' band.

Description	**Value**
Readout rate (fps/MHz)	1/1
Read noise (e^-)	6
Active pixels	1024×1024
Pixel size (μm^2)	13×13
Well depth	90,000
QE	>0.90
Operating Temperature (C°)	-20 to 30
Storage Temperature (C°)	-25 to 50
Cooling Method	Thermo-electric

Table 4: Details for the iXon3 888 EMCCD. The values given red are true for the iXon Ultra 888, but haven't been confirmed for the iXon3 888

Description	**Value**
Readout rate (fps)	35
Active pixels	1280×960
Pixel size (μm^2)	3.75×3.75
Well depth	13,000
QE	<0.80
Operating Temperature (C°)	-5 to 45
Storage Temperature (C°)	-20 to 60
Cooling Method	None

Table 5: Details for the ASI 120 mm guide camera.

Description	OC	DAC
Motherboard	Intel Xeon E-2100 MB	
Processor	Intel Core i3-9100, 3.6 GHz, 4-core	AMD EPYC™ 7453, 2.75 GHz, 28-core
OS	Windows 10 Pro	Linux
Storage capacity	2×512 GB	4 × 10 TB
Memory/swap	—	8×16 GB
Power	350 W	500 W
Dimensions	17.2"×1.7"×14.5"	17.2"×1.7"×23.5"

Table 6: Information on the operations computer (OC) and data analysis and storage computer (DAC) for Flarescope.

2.7 CPUs

Flarescope will have two dedicated computers: one for controlling the operations of the observatory (all subsystems listed in table 7 besides the analysis subsystem) (OC) and one for data analysis and storage (DAC). The OC will have a Windows operating system (OS) to support the software for controlling the dome, mount, and focuser and the DAC will have a Linux OS. The DAC will have four, 10 TB hard drives configured with RAID 10 to ensure all data are mirrored locally for backup. Assuming 4 MB file sizes and 6 hours of observing per night, then the DAC should be able to support 7-8 months of 1 s resolution images. Unusual data (observations with an high number of flagged images or data where a flare is identified) will be inspected by eye regularly and all data will be consolidated to a 10 s time resolution on a monthly basis to accommodate more observations before doing a data dump.

2.7.1 HVAC

Because the temperatures at Palomar are within the temperature restrictions of the EMCCD and guide camera, the CPUs are what set the HVAC requirements. Because only the CPUs need to be kept cool, rather than getting an HVAC setup to keep the entire interior of the dome cool, we will be getting an air conditioned enclosure specifically for the CPUs. This enclosure will be 4X NEMA rated and capable of supporting the anticipated $\sim$ 150 W ($\sim$ 500 BTU/hr) heat load within the -5°C to 30°C ambient temperature range expected at Palomar.

3 Dome

The dome will be the Astrohaven 12.5-1 dome (see Figure 3). This is a 12.5', remotely controlled, belt driven, clamshell dome. The two sides of the dome can be controlled independently of each other, allowing for fine control of the exposure of the dome interior (*e.g.* the telescope) to the environment. Although there is human-machine interface available on the dome for manual control, we will be using a MODBUS driver that makes remote control through a CPU possible.

4 Site

4.1 Selection

The Palomar Observatory has four available sites for consideration for Flarescope. We intend to put Flarescope at a site south of the the Widefield Infrared Transient Explorer (WINTER) and north of the Palomar 200". Although the site north of WINTER would be lower cost in terms of site excavation, there is a weather tower that provides a 50° elevation obstruction; the highest elevation obstruction in the southern site is 22°.

4.2 Infrastructure

Because the OC and DAC will be stored in a temperature controlled enclosure in the dome instead of a separate shed, our infrastructure concerns are limited to power, internet, and road accessibility to the dome and the electronics within. The site is 160 feet from both a paved road and the WINTER gravel path and will be pulling power resources from the WINTER site that is 220 feet away.

4.3 Weather Station

We will be using the Vantage Vue weather station for weather forecasting and to monitor the temperature, pressure, wind speed and direction, cloud coverage, humidity, and recent rainfall. The Vantage Vue sends data to a separate console that will be kept in the dome. Data from the console can then be accessed by the CPUs. Additionally, we will be using weather information from the Palomar 200" telescope; if they identify poor observing conditions when the Vantage Vue has not, Flarescope will keep the dome closed to be certain the equipment is safe.

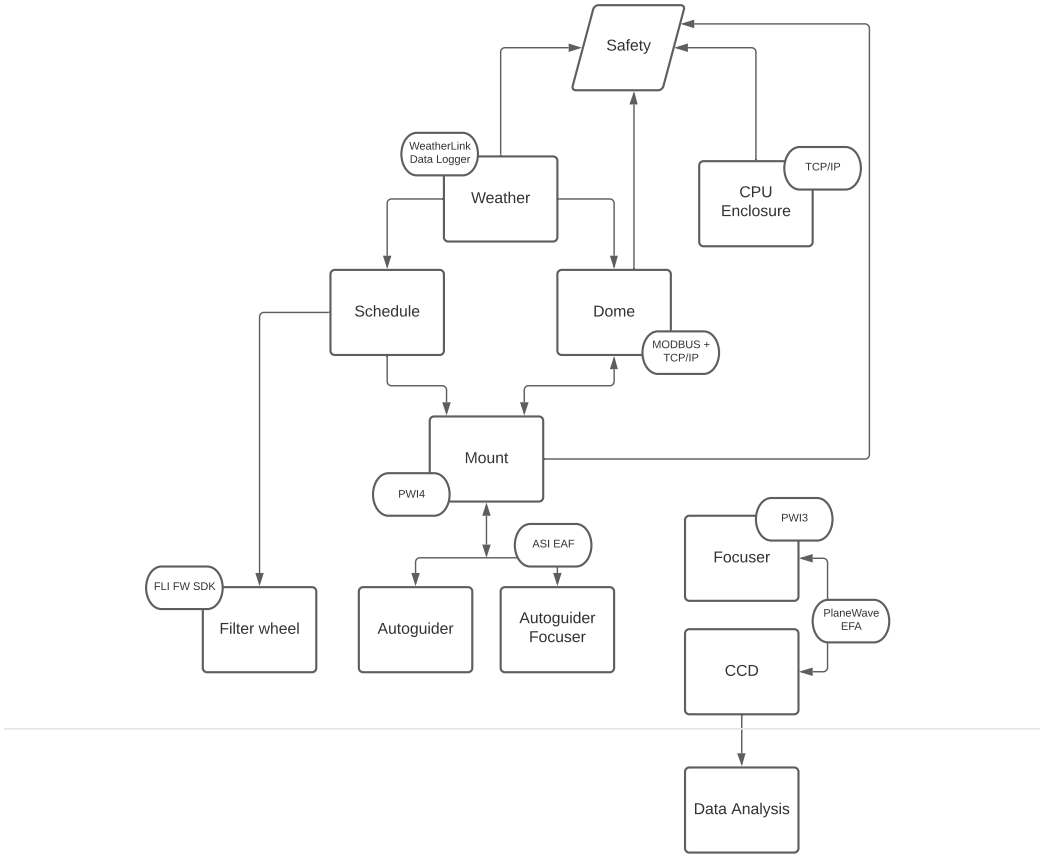

Figure 6: The path for communications between subsystems, assuming that the Interfacing subsystem is acting as the mediator in the paths. Not shown here is that the Safety subsystem will be able to communicate with all others to halt observations during dangerous situations. Additionally, the CPU enclosure, weather, dome, mount, filter wheel, and data analysis subsystems will be able to communicate with the Reporting subsystem to update a website with information on the status of the observatory.

Subsystem	Description
Weather	Responsible for identifying when the weather is conducive for observing. Communicates with the dome subsystem to open when appropriate and close when necessary. Will give regular reports on the status of the weather so that manual overrides to the dome can be given if necessary.
Dome	Responsible for opening shutters to the appropriate extent to perform observations as well as block out wind. It will also make sure the dome is closed after observations. It will communicate with the safety subsystem to provide auditory and visual alerts when it is opening/closing for the evening/morning as well as when it will be changing orientation significantly to accommodate a new target. It will send an alert if the dome gets stuck or experiences other errors and will regularly report on the status of the dome.
Scheduling	Responsible for making an observing schedule for the night based on object priority, elevation, and its proximity to the Moon (as well as identifying the phase of the Moon and consequently identifying how close is "too close" *e.g.* an object can be closer to a new moon than a full moon).
HVAC	Responsible for reporting the temperature of the enclosure of the CPUs and communicating with the safety subsyste to send alerts and halting observations if a critical temperature is reached.
Mount	Responsible for slewing to the appropriate target and carrying out the observations. Will report on which target is being observed, direction of pointing, and will communicate with the safety subsystem to provide visual and auditory alerts for when the telescope is about to slew to a new object.
Focuser	Responsible for rotating the focuser to orient the CCD to provide the necessary FOV for doing observations.
Filter wheel	Responsible for setting the filter wheel to the appropriate diffuser or no diffuser at all. Also responsible for setting the correct Sloan filter depending on the science of the observation. It will report which filters are being used and which diffuser if any is in use.
Autoguiding	Responsible for identifying a guide star for each new field that the telescope slews to and maintaining sub-pixel tracking throughout the night.
Analysis	Responsible for performing data reduction and photometry on the images produced by the telescope subsystem as well as identifying flares. Will update with the latest co-added, mmag precision image and update the light curve for the object. Will also communicate with the reporting subsystem to send alerts for the identified flares.
Safety	Will be responsible for communicating/coordinating with the other subsystems; once an error or safety concern has been identified, it will be responsible for making the necessary alerts or halting observations.
Interfacing	Responsible for communicating between the Python scripts in the pipeline and the other programs needed for observing (*e.g.* PWI4)
Reporting	Will be responsible for communicating with the other subsystems in order to update the online server with the relevant information.

Table 7: A list of the Flarescope subsystems and descriptions of their roles.

5 Software Requirements

5.1 Data Analysis Pipeline

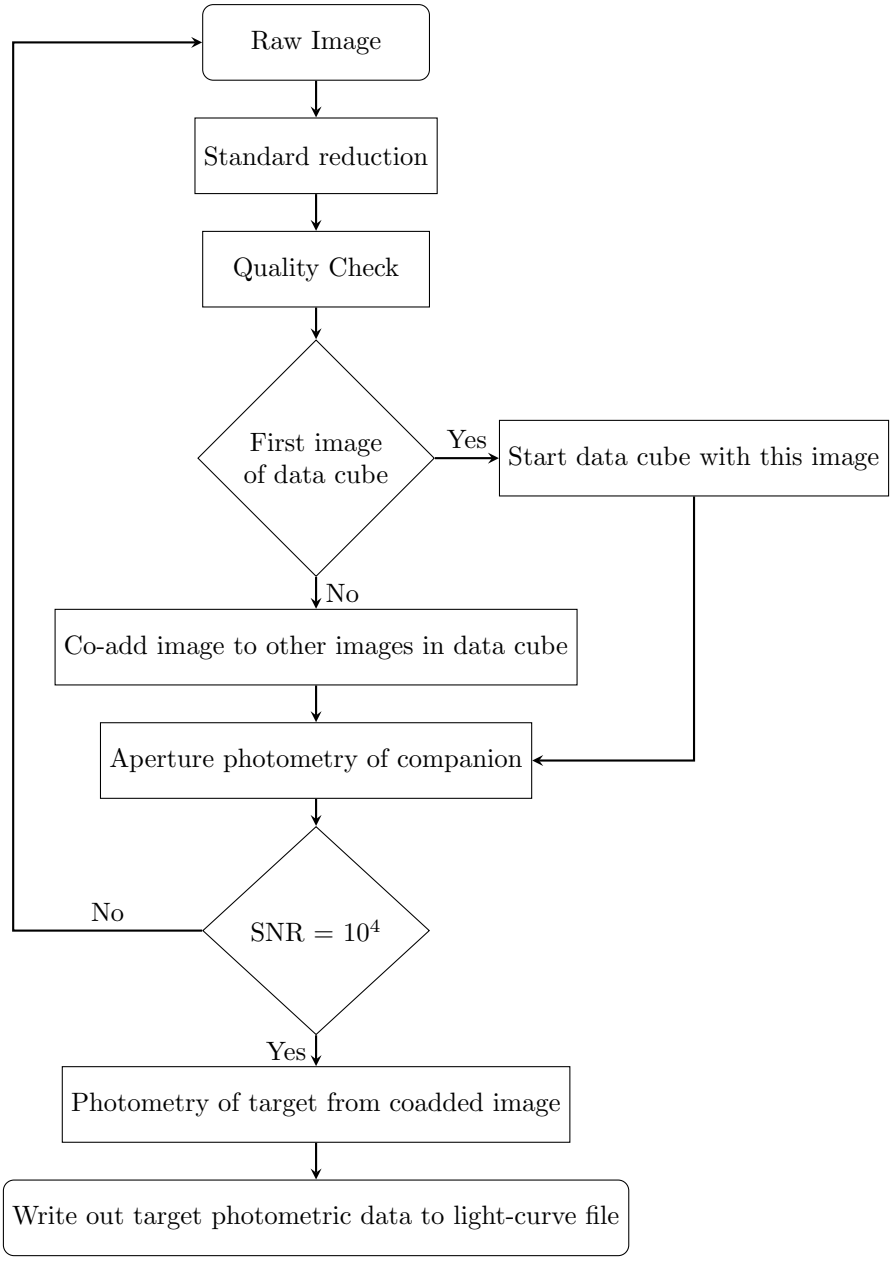

The data analysis subsystem of Flarescope will be doing reduction and differential photometry on every image with `photutils` [1] as soon as the image is produced. Images will be coadded until mmag precision from the companion star is reached, at which point differential photometry will be performed for the target star (see flowchart). All information on the reduced image (data, header, companion flux and noise, and associated file names of the raw image and flats, darks, and biases used) will be stored in the data cube that used the image. The differential flux and noise of the target star from the final coadded image in the data cube will be written out to a separate light curve file. This pipeline is based on the PyChimera pipeline developed by Dr. Navtej Singh for the CHIMERA instrument. Dr. Singh has experience developing roboticized observatories and will be collaborating via JROC in the automatizing of the Flarescope system.

Flare identification will be done through an adapted version of a pipeline developed by Mike Greklek-McKeon. This pipeline was originally produced for identifying flares from TESS data and thus needs to be modified to accommodate on-the-fly flare identification. Information on flares identified by this pipeline (*e.g.* the start and end time and integrated flux) will be written out to a separate file that will be reported so that further inspection can be done.

6 Timeline

The Flarescope team intends to begin purchasing the equipment summarized in table 3 immediately after the design review. Due to the past and continuing status of the COVID-19 pandemic and the impact it has had on the optical instrument market, the anticipated delivery times are a major unknown. There is an interface control document continually being developed with Palomar staff to resolve the schedule and finer detail requirements. We plan to have the dome and CDK 400 observatory by early 2022 and for all subsystems to be integrated by the end of 2022 so that observations can begin in early 2023.

References

[1] Larry Bradley, Brigitta Sipőcz, Thomas Robitaille, Erik Tollerud, Zè Vinícius, Christoph Deil, Kyle Barbary, Tom J Wilson, Ivo Busko, Hans Moritz Günther, Mihai Cara, Simon Conseil, Azalee Bostroem, Michael Droettboom, E. M. Bray, Lars Andersen Bratholm, P. L. Lim, Geert Barentsen, Matt Craig, Sergio Pascual, Gabriel Perren, Johnny Greco, Axel Donath, Miguel de Val-Borro, Wolfgang Kerzendorf, Yoonsoo P. Bach, Benjamin Alan Weaver, Francesco D'Eugenio, Harrison Souchereau, and Leonardo Ferreira. astropy/photutils: 1.0.0, September 2020.

[2] M. Coffaro, B. Stelzer, S. Orlando, J. Hall, T. S. Metcalfe, U. Wolter, M. Mittag, J. Sanz-Forcada, P. C. Schneider, and L. Ducci. An X-ray activity cycle on the young solar-like star Eridani. , 636:A49, April 2020.

[3] G. A. Dulk. Radio emission from the sun and stars. , 23:169–224, January 1985.

[4] L. Fletcher, I. G. Hannah, H. S. Hudson, and T. R. Metcalf. A TRACE White Light and RHESSI Hard X-Ray Study of Flare Energetics. , 656(2):1187–1196, February 2007.

[5] H. E. Fröhlich. The differential rotation of ărepsilon Eri from MOST data. *Astronomische Nachrichten*, 328(10):1037, December 2007.

[6] William Huggins and Margaret Lindsay Huggins. On a New Group of Lines in the Photographic Spectrum of Sirius. *Sidereal Messenger*, 9:318–319, August 1890.

[7] V. Kornilov, M. Sarazin, A. Tokovinin, T. Travouillon, and O. Voziakova. Comparison of the scintillation noise above different observatories measured with MASS instruments. , 546:A41, October 2012.

[8] M. Kretzschmar. The Sun as a star: observations of white-light flares. , 530:A84, June 2011.

[9] Nicholas M. Law, Octavi Fors, Jeffrey Ratzloff, and Philip J. Wulfken. The Evryscope: the first full-sky gigapixel-scale telescope. In *American Astronomical Society Meeting Abstracts #225*, volume 225 of *American Astronomical Society Meeting Abstracts*, page 202.07, January 2015.

[10] Andrew W. Mann, Eric Gaidos, and Greg Aldering. Ground-Based Submillimagnitude CCD Photometry of Bright Stars Using Snapshot Observations. , 123(909):1273, November 2011.

[11] Dimitri Mawet, Lea Hirsch, Eve J. Lee, Jean-Baptiste Ruffio, Michael Bottom, Benjamin J. Fulton, Olivier Absil, Charles Beichman, Brendan Bowler, Marta Bryan, Elodie Choquet, David Ciardi, Valentin Christiaens, Denis Defrère, Carlos Alberto Gomez Gonzalez, Andrew W. Howard, Elsa Huby, Howard Isaacson, Rebecca Jensen-Clem, Molly Kosiarek, Geoff Marcy, Tiffany Meshkat, Erik Petigura, Maddalena Reggiani, Garreth Ruane, Eugene Serabyn, Evan Sinukoff, Ji Wang, Lauren Weiss, and Marie

Ygouf. Deep Exploration of Eridani with Keck Ms-band Vortex Coronagraphy and Radial Velocities: Mass and Orbital Parameters of the Giant Exoplanet. , 157(1):33, January 2019.

[12] J. Osborn, D. Föhring, V. S. Dhillon, and R. W. Wilson. Atmospheric scintillation in astronomical photometry. , 452(2):1707–1716, September 2015.

[13] Rachel A. Osten and Scott J. Wolk. Connecting Flares and Transient Mass-loss Events in Magnetically Active Stars. , 809(1):79, August 2015.

[14] I. Rueedi, S. K. Solanki, G. Mathys, and S. H. Saar. Magnetic field measurements on moderately active cool dwarfs. , 318:429–442, February 1997.

[15] Gudmundur Stefansson, Suvrath Mahadevan, Leslie Hebb, John Wisniewski, Joseph Huehnerhoff, Brett Morris, Sam Halverson, Ming Zhao, Jason Wright, Joseph O'rourke, Heather Knutson, Suzanne Hawley, Shubham Kanodia, Yiting Li, Lea M. Z. Hagen, Leo J. Liu, Thomas Beatty, Chad Bender, Paul Robertson, Jack Dembicky, Candace Gray, William Ketzeback, Russet McMillan, and Theodore Rudyk. Toward Space-like Photometric Precision from the Ground with Beam-shaping Diffusers. , 848(1):9, October 2017.

[16] Jonathan J. Swift, Michael Bottom, John A. Johnson, Jason T. Wright, Nate McCrady, Robert A. Wittenmyer, Peter Plavchan, Reed Riddle, Philip S. Muirhead, Erich Herzig, Justin Myles, Cullen H. Blake, Jason Eastman, Thomas G. Beatty, Stuart I. Barnes, Steven R. Gibson, Brian Lin, Ming Zhao, Paul Gardner, Emilio Falco, Stephen Criswell, Chantanelle Nava, Connor Robinson, David H. Sliski, Richard Hedrick, Kevin Ivarsen, Annie Hjelstrom, Jon de Vera, and Andrew Szentgyorgyi. Miniature Exoplanet Radial Velocity Array (MINERVA) I. Design, Commissioning, and First Science Results. *Journal of Astronomical Telescopes, Instruments, and Systems*, 1:027002, April 2015.

[17] Jr. Villanueva, Steven, B. Scott Gaudi, Richard W. Pogge, Jason D. Eastman, Keivan G. Stassun, Mark Trueblood, and Patricia Trueblood. DEdicated MONitor of EXotransits and Transients (DEMONEXT): System Overview and Year One Results from a Low-cost Robotic Telescope for Followup of Exoplanetary Transits and Transients. , 130(983):015001, January 2018.

[18] Thomas N. Woods, Francis G. Eparvier, Juan Fontenla, Jerald Harder, Greg Kopp, William E. McClintock, Gary Rottman, Byron Smiley, and Martin Snow. Solar irradiance variability during the October 2003 solar storm period. , 31(10):L10802, May 2004.